Interaction of Mesoporous Silica Nanoparticles with Human Red Blood Cell Membranes: Size and Surface Effects

Yannan Zhao, Xiaoxing Sun, Guannan Zhang, Brian G. Trewyn,* Igor I. Slowing,* and Victor S.-Y. Lin†

Department of Chemistry, U.S. Department of Energy Ames Laboratory, Iowa State University, Ames, Iowa 50011-3111, United States. †Deceased on May 4, 2010.

ABSTRACT The interactions of mesoporous silica nanoparticles (MSNs) of different particle sizes and surface properties with human red blood cell (RBC) membranes were investigated by membrane filtration, flow cytometry, and various microscopic techniques. Small MCM-41-type MSNs (~100 nm) were found to adsorb to the surface of RBCs without disturbing the membrane or morphology. In contrast, adsorption of large SBA-15-type MSNs (~600 nm) to RBCs induced a strong local membrane deformation leading to spiculation of RBCs, internalization of the particles, and eventual hemolysis. In addition, the relationship between the degree of MSN surface functionalization and the degree of its interaction with RBC, as well as the effect of RBC–MSN interaction on cellular deformability, were investigated. The results presented here provide a better understanding of the mechanisms of RBC–MSN interaction and the hemolytic activity of MSNs and will assist in the rational design of hemocompatible MSNs for intravenous drug delivery and *in vivo* imaging.

KEYWORDS: mesoporous silica nanoparticle (MSN) · size · surface functionality · red blood cell (RBC) membrane · interaction · internalization · deformability

Recent advancements in particle size and morphology control of mesoporous materials have led to the creation of nano- and submicrometer-sized mesoporous silica nanoparticles (MSNs).[1−5] The MSN materials with well-ordered cylindrical pore structures, such as MCM-41 and SBA-15, have attracted special interest in the biomedical field.[1] The large surface areas and pore volumes of these materials allow the efficient adsorption of a wide range of molecules, including small drugs,[6−10] therapeutic proteins,[11−13] antibiotics,[14,15] and antibodies.[16] Therefore, these materials have been proposed for use as potential vehicles for biomedical imaging, real-time diagnosis, and controlled delivery of multiple therapeutic agents.[6−8,10,17−25]

Despite the considerable interest in the biomedical applications of MSNs, relatively few studies have been published on the biocompatibility of the two most common types of MSNs (MCM-41 and SBA-15).[26−29] Asefa and co-workers reported that the cellular bioenergetics (cellular respiration and ATP levels) were inhibited remarkably by large SBA-15 nanoparticles, but the inhibition was greatly reduced by smaller MCM-41-type nanoparticles.[26] These differences in the disruption of cellular bioenergetics are believed to be caused by the different surface areas, number of surface silanol groups, and/or particle sizes of both types of material. A recent study by Kohane and collaborators on the systemic effects of MCM-41 (particle size ~150 nm) and SBA-15 (particle size ~800 nm) MSNs in live animals revealed interesting findings regarding their biocompatibility.[27] While large doses of mesoporous silicas administered subcutaneously to mice appear to be relatively harmless, the same doses given intravenously or intraperitoneally were lethal.[27] A possible reason for the severe systemic toxicity of MSNs when injected intravenously could be the interactions of the nanoparticles with blood cells.

Our initial studies on the biocompatibility of MCM-41-type MSNs with red blood cells (RBCs), the dominant (99%) cell type in blood, suggested that this material was innocuous in comparison to the highly hemolytic amorphous silica.[30] These results were later confirmed by Lin and Haynes, who demonstrated that the hemocompatibility of MSNs also depended on the size of the nanoparticles.[31] These findings were mainly based on hemolysis assays performed by UV–vis spectroscopy. The lack of hemolysis, however, does not necessarily warrant the absence of interactions between the particles and the RBCs, which could lead to more subtle side effects. Such side effects could eventually be the ones responsible for the enhanced systemic toxicity observed upon intravenous injection of these materials.[27] Therefore, an in-depth study of other possible biological side effects of these materials must be performed if they are intended to be applied as vehicles for drug delivery.

* Address correspondence to bgtrewyn@iastate.edu, islowing@iastate.edu.

Received for review November 12, 2010 and accepted January 24, 2011.

Published online February 04, 2011
10.1021/nn103077k

In general, our knowledge of the biocompatibility, bioretention, and biodistribution of MSNs does not match with the rapid pace of research on their syntheses in numerous forms and structures. To date, efforts have focused predominantly on exploiting multifunctional nanoparticles as intravascular drug carriers with different particle sizes ranging from a few tens of nanometers[4,24,32] up to hundreds of nanometers,[3,5] various pore diameters ranging from 2 to 10 nm,[5,11,33] and assorted surface functionalities from small organic groups (*e.g.*, amino,[34,35] carboxyl,[35] thiol,[35] phosphate,[19] *etc.*) to large molecules (*e.g.*, dendrimers,[36] polyethyleneimine (PEI),[25,37] poly(ethylene glycol) (PEG),[38] phospholipids,[39] *etc.*). Unfortunately, these endeavors are limited by a poor understanding of particle interactions with cells in circulation.

Herein, we report our investigations on the interactions of the two most common types of MSNs (MCM-41 and SBA-15) with RBC membranes using fluorescence and electron microscopies and cell biology techniques. In addition to studying the effects of particle size and surface area on the hemolytic behavior of MSNs, we explored the effects that the chemical nature and degree of surface functionalization of the particles have on their interactions with RBCs. Understanding these effects will not only offer a guide for the rational design of biocompatible particles but also provide an insight into how to control the circulation properties of MSNs in the bloodstream. In fact, a prolonged circulation of polymeric nanoparticles has been recently demonstrated by means of their noncovalent attachment to the RBC membrane.[40] Attachment to the RBC membrane, however, may affect one of its most important properties, namely, its deformability (*i.e.*, the ability of an erythrocyte to deform so it can flow through microcirculation). To the best of our knowledge, this problem has not yet been addressed for any drug delivery system. In this work, we examined the effect of RBC−MSN interactions on membrane deformability by the Nucleopore filtration technique[41] and established how size and surface properties can alter this important property. Overall, we propose three fundamental criteria to assess the hemocompatibility of nanoparticles: (1) hemolytic potential, (2) propensity to induce RBC membrane deformation or morphological alteration, and (3) tendency to impair RBC deformability. The evaluation of these conditions will enable a more adequate estimation of the hemocompatibility of many types of nanomaterials. This study suggests a minimal set of criteria that must be met before performing *in vivo* studies involving the intravascular administration of nanoparticles.

RESULTS AND DISCUSSION

Size- and Surface-Dependent MSN Interaction with RBC Membranes. While particle size effect of MCM-41-type MSNs has already been established with larger particles producing lower hemolysis on RBC,[31] the question remains whether the typically larger SBA-15-type MSNs are hemocompatible. A more critical issue is that the mechanism of how MSNs of different sizes and surface areas correlate and contribute to their hemocompatibility is unclear, although several biological rationales have been suggested.[30,31] To address these questions, we prepared two types of MSNs: MCM-41 and SBA-15, as described in the Methods section. Scanning electron microscopy (SEM) and transmission electron microscopy (TEM) images showed particle sizes of 100 to 200 nm for the MCM-41-type MSNs (referred to as *s*-MSN, Figure 1a,d) and ~600 nm by ~300 nm for the SBA-15-type MSNs (referred as *l*-MSN, Figure 1b,e). The hydrodynamic particle size distributions of the materials suspended in phosphate-buffered saline (PBS) (100 μg mL^{-1}) were determined by dynamic light scattering (DLS), giving average sizes of 122 nm for *s*-MSN and 531 nm for *l*-MSN (Figure 1c). XRD patterns showed that both *s*-MSNs and *l*-MSNs exhibit 2D hexagonal pore arrangements (Figure 1f).

The hemolysis assay was used to evaluate the hemolytic behaviors of *s*-MSN and *l*-MSN on human RBCs. Human RBCs were first isolated by centrifugation and purified by five successive washes with sterile isotonic PBS, then diluted to 5% hematocrit with PBS before incubating with MSN suspensions of various concentrations. Controls were prepared in the same manner as the above RBC samples except adding water (positive control) and PBS (negative control) instead of the MSN suspensions. After a 2 h incubation at room temperature, the samples were spun down for the detection of hemoglobin released from hemolyzed RBCs. Surprisingly, contrary to the recently reported trend regarding size,[31] MSNs with larger particle size exhibited a higher hemolytic activity than the small particles (Figure 2). The hemolytic activity of *l*-MSNs was first observed at 50 μg mL^{-1} with 5% hemolysis detected, while a good hemocompatibility (<2% hemolysis) of *s*-MSN was confirmed at concentrations as high as 100 μg mL^{-1}. While a larger particle size may be preferable for hemocompatible MSNs below 225 nm,[31] increasing particle size of MSNs beyond this range will not necessarily improve the hemocompatibility as one might intuitively expect. In addition to particle size, other factors such as the surface area are also expected to affect the hemolytic potential of MSNs.

To elucidate the mechanism of the observed difference in hemolysis and investigate the underlying particle size and surface effects, the interaction of MSNs with RBCs were visualized by SEM (Figure 3) and TEM (Figure 4). A small proportion of *s*-MSNs were found to adsorb to the surface of RBC. The cell membrane did not show any alteration upon particle binding, and RBCs maintained normal biconcave shape compared to control RBCs (Figure 3B and Figure 4 top). In contrast, a large proportion of *l*-MSNs attached to RBC membranes and induced a

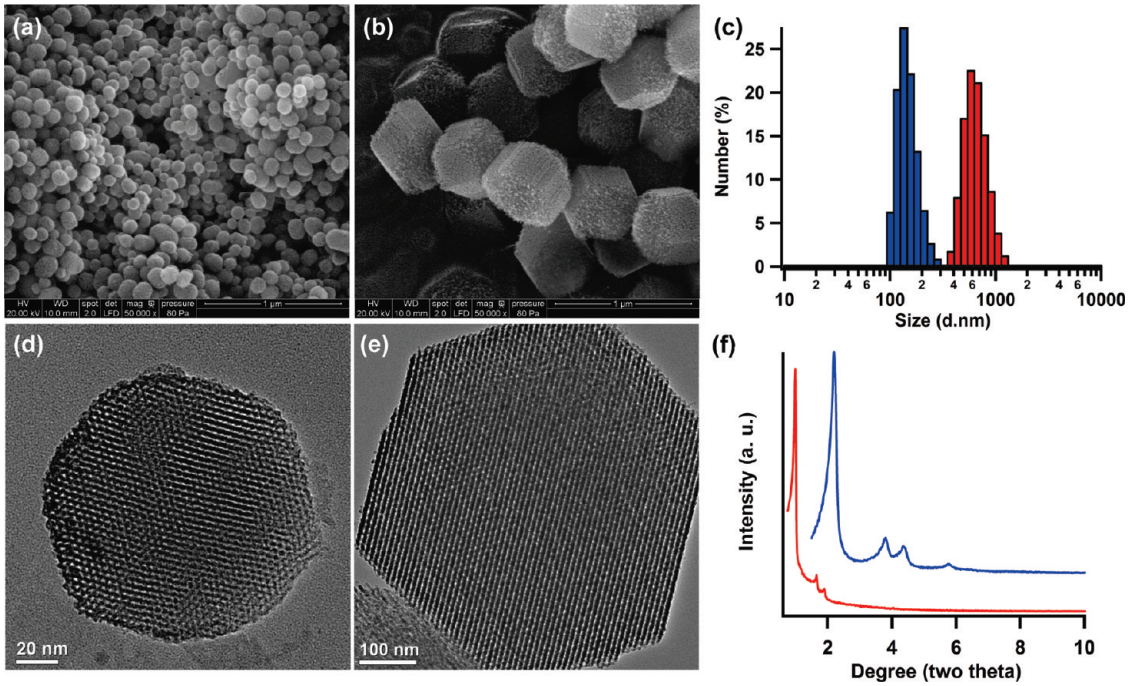

Figure 1. Scanning electron (top) and transmission electron (bottom) images of (a,d) *s*-MSN and (b,e) *l*-MSN. (c) Hydrodynamic size distributions of *s*-MSN (blue) and *l*-MSN (red) suspended in PBS (100 μg mL^{-1}) measured by dynamic light scattering. (f) X-ray diffraction patterns of *s*-MSN (blue) and *l*-MSN (red).

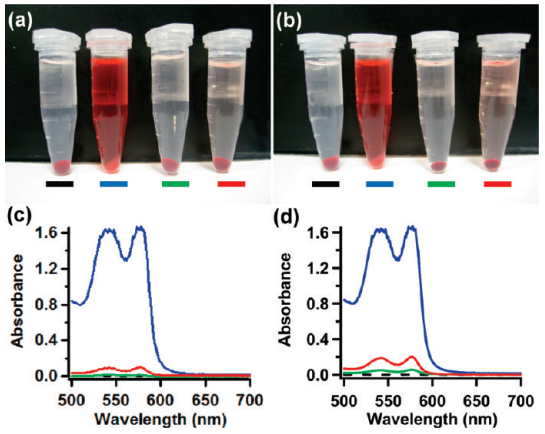

Figure 2. Hemolysis assay for *s*-MSN (green lines) and *l*-MSN (red lines), using water as a positive control (blue lines) and PBS as a negative control (dashed black lines). The materials were suspended at 50 (a,c) and 100 μg mL^{-1} (b,d). The mixtures were centrifuged to detect the presence of hemoglobin in the supernatant visually (a,b) and by absorption at 541 nm (c,d).

strong local membrane deformation, which frequently resulted in particle encapsulation by RBCs (Figure 3C and Figure 4 bottom). The membrane wrapping around *l*-MSNs led to an echinocytic (spiculated) shape transformation of RBCs and a reduction in the ratio of surface area to volume.[42] This inability to maintain their normal surface area and control their cell volume can ultimately lead to the destruction of these cells,[42] which explains the observed high hemolytic activity of *l*-MSNs.

Two main processes are involved in the interaction of MSN with the membrane of RBC: (1) binding of the silanol-rich surface of MSNs with the phosphatidyl choline-rich RBC membrane,[30] and (2) bending of the RBC membrane to adapt to the rigid surface of MSNs (Scheme 1).[43−47] The occurrence of the interaction depends on whether the amount of energy released from the binding of the MSNs with the RBC membrane (E_i) is able to overcome the amount of free energy required to bend the membrane and adapt to the surface of MSNs (E_b). The former energy is associated with the external surface area (*i.e.*, accessible silanols) of MSN,[30] while the latter is proportional to the curvature or inversely proportional to the square of the radius (r) of the particle.[43,44,47] The external surface areas of *s*-MSNs and *l*-MSNs, calculated from the *t* plots of their N_2 adsorption isotherms,[48] were 81.6 and 155.4 m^2 g^{-1}, respectively. The relatively large external surface area of *l*-MSN (40% of total surface area) in comparison to that of *s*-MSN (8% of total surface area) implies that *l*-MSN can have a larger binding energy (E_i) available for pulling the membrane to the particle surface. In addition, since surface curvature decreases with particle size, the bending energy required to wrap the large particles (E_b) is lower than the one needed to wrap the smaller particles.[43] This combination makes membrane wrapping and engulfment of *l*-MSN thermodynamically favorable. On the contrary, in order for the RBC membranes to wrap around smaller *s*-MSNs, they would have to attain a larger curvature (steeper angles over smaller areas) than they need for wrapping around the larger particles.[43] This would require investing a much higher E_b compared to the small amount of E_i, which thermodynamically prevents the membrane deformation

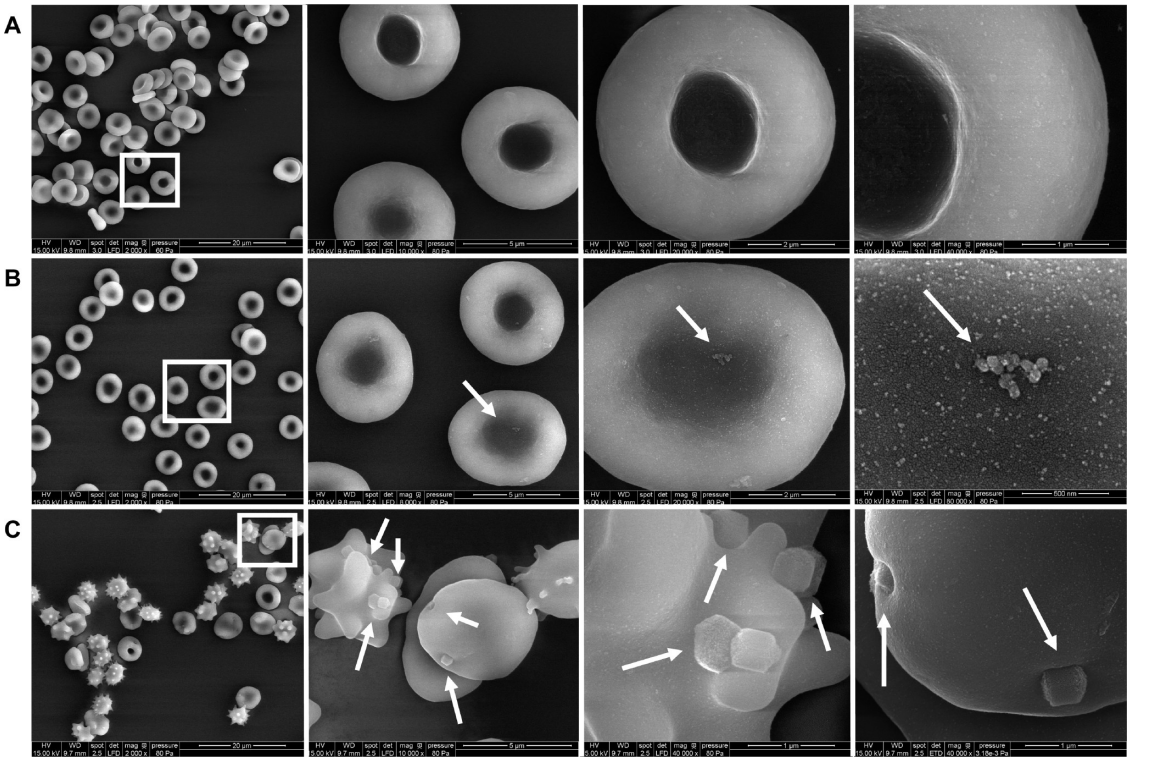

Figure 3. Scanning electron images of RBCs (5% hematocrit) incubated for 2 h at room temperature with (A) PBS as control, (B) 100 μg mL^{-1} of *s*-MSN, and (C) 100 μg mL^{-1} of *l*-MSN. Images increase in magnification from left to right with features highlighted with white squares or arrows. The nanoparticles attached on the cell surface are distinguished by the particle shape and surface textural difference between the particles and RBCs. (Additional high-magnification images are shown in Figure S2 in Supporting Information.)

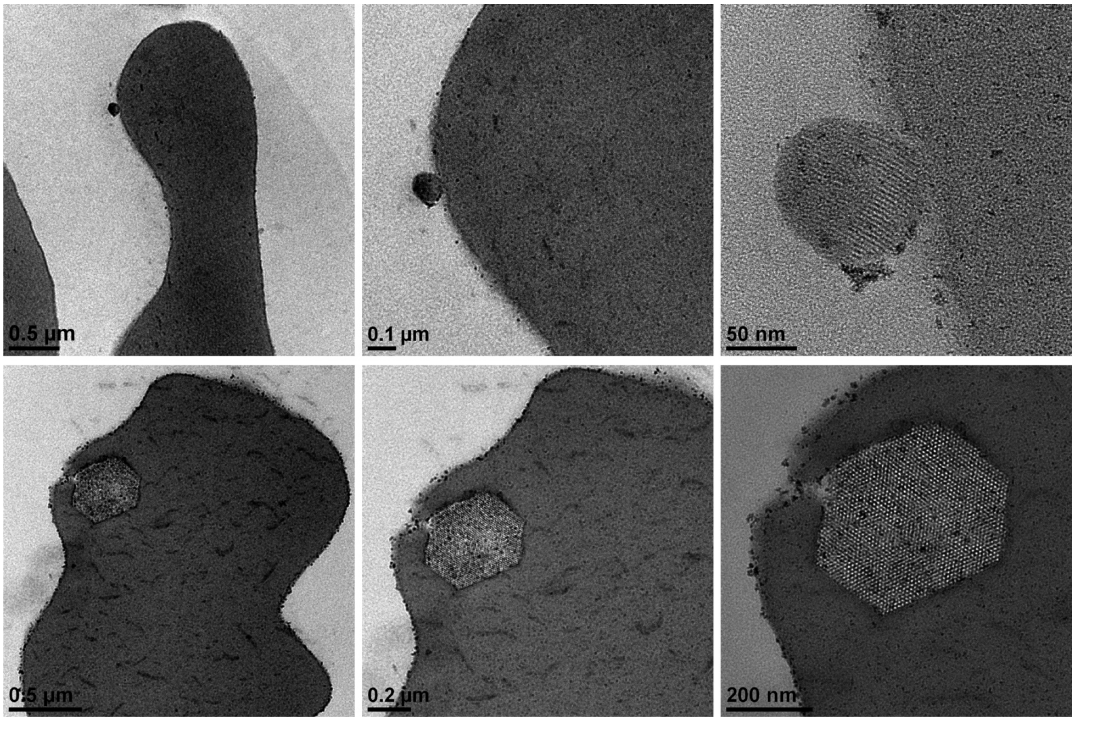

Figure 4. Transmission electron images of RBCs (5% hematocrit) incubated for 2 h at room temperature with 100 μg mL^{-1} *s*-MSN (top) and *l*-MSN (bottom). Images increase in magnification from left to right. The presence of MSNs is confirmed by the visible pores in the higher magnification micrographs.

or engulfment of *s*-MSN by RBC and explains the lower hemolytic activity of *s*-MSNs. Similar explanations on the effect of particle size on membrane wrapping have been reported elsewhere.[43,44] Hence, the interaction of MSNs

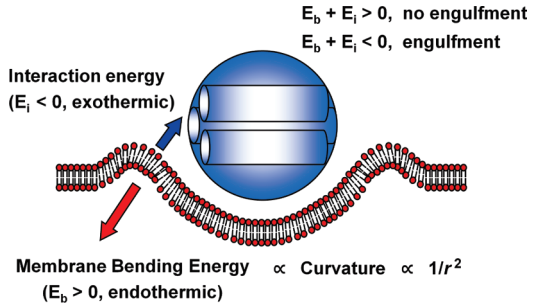

Scheme 1. Schematic illustration of the size- and surface-dependent interaction of MSN and RBC membrane. MSN with radius *r* can be wrapped around or engulfed by RBC if the energy (E_i) released from the RBC−MSN interaction is greater than the energy (E_b) required for membrane bending.

with RBC membranes and the hemolytic activity depend on not only particle size but also their external surface area, as well.

Size- and Surface-Dependent Engulfment of MSNs by RBCs. Though the *in vitro* endocytosis of MSN has been systematically investigated with various mammalian cell lines,[4,11,17,34,36,49−52] little is known about the uptake of nanoparticles by RBCs. This is partly because the interactions between RBC and MSN are still poorly understood. Before investigating the internalization of MSNs by RBC, it is necessary to establish the concentration at which the plasma membrane maintains its integrity and RBCs retain normal biconcave shape. To do so, the RBCs were incubated with *l*-MSNs at different concentrations, and the hemolytic effects as well as the resulting cell morphologies were examined by UV−vis spectroscopy (Figure S3 in Supporting Information) and SEM (Figure S4). The hemolysis percentage of RBCs increased from 1 to 11% as the concentration of *l*-MSN increased from 20 to 100 μg mL^{-1}, and growing proportions of spiculated RBCs were observed with increasing concentrations of *l*-MSN. As shown in Figure S4, almost 90% of RBCs exhibited spiculated shape with 100 μg mL^{-1} of *l*-MSN. The proportion of spiculated RBCs decreased to 50% when 50 μg mL^{-1} of *l*-MSN was used. Interestingly, only minor shape modifications (less than 10% spiculated cells) in RBCs were observed after incubation with 20 μg mL^{-1} of *l*-MSN, even if many particles were adsorbed to the membranes or underwent internalization (Figure S4, left). Therefore, the cellular uptake process was examined at a concentration of 20 μg mL^{-1} of *l*-MSN (Figure 5). It should be noted that the images in Figure 5 correspond to different cells at different stages of nanoparticle encapsulation. A plausible interpretation of our observations is as follows. The particle interacts with an initially flat cell membrane. Driven by a local reduction in free energy (Scheme 1), the phospholipids in the immediate neighborhood of the site of contact are drawn to the surface of the particle, leading to membrane wrapping and eventual encapsulation. Such internalization is different from phagocytosis or endocytosis because it appears to be driven by the balance of two opposing forces rather than by an active uptake of nutrients by the cell. It should be stressed that even if almost no hemolysis or spiculation is observed at this concentration we cannot yet exclude the potential side effects of the internalization of *l*-MSN into RBC. Nevertheless, this preliminary study on MSN engulfment by RBC is an important step toward establishing the plausibility of using MSNs as tools for the treatment of RBC-related diseases or intravascular drug delivery. We are currently conducting more studies to understand and control the internalization of MSNs and the delivery of therapeutic agents into RBCs to be published in subsequent manuscripts.

Surface Functionality Effects on RBC−MSN Interaction. The results from the size- and surface-dependent interactions of MSNs with RBCs have demonstrated a superior hemocompatibility of *s*-MSNs over *l*-MSNs. This does not imply, however, that *s*-MSNs lack any interaction with the membranes of RBCs. While the interactions of MSNs with the membranes of RBCs are known to be dependent on the presence of silanol groups on the surface of the particles,[30,31] there is no quantitative information on the magnitude of this association. Given the interest of utilizing *s*-MSNs for intravenous drug delivery, it is necessary to be able to measure and control the degree of the above-mentioned interactions and, thus, controlling the circulation of the particles in the bloodstream.[40,53]

To study these interactions, *s*-MSNs were first labeled with fluorescein isothiocyanate (FITC), which enabled their tracking by flow cytometry and confocal fluorescence microscopy. FITC-*s*-MSNs were then functionalized with different amounts of aminopropyl (AP), polyethylene glycol (PEG), and carboxyl (CA) groups, as described in the Methods section. These functionalized materials are referred as AP_x-FITC-*s*-MSN, PEG_x-FITC-*s*-MSN, and CA_x-FITC-*s*-MSN, respectively, where the subscript *x* corresponds to the number of mmol introduced per gram of material. The amount of functional groups (AP, PEG, and CA) grafted on MSNs was quantified by TGA shown in the bottom of Figure S5 of the Supporting Information and summarized in Table S1. The quantification of nanoparticle attachment to the membrane of RBCs was performed by flow cytometry. Diluted suspensions of RBCs (5×10^6 cells mL^{-1}) were mixed with equal volumes of nanoparticle suspensions to reach a final concentration of 10 μg mL^{-1} of MSNs and incubated at room temperature for 2 h before flow cytometry analysis. As shown in Figure 6, the functionalized nanoparticles exhibited lower affinity to RBC than FITC-*s*-MSNs; furthermore, the affinity decreased with increasing degree of functionality. This trend was observed for each functionalized material, independent of the surface charge. In particular, AP and PEG groups (~25% of RBC bound with $AP_{1.5}$-FITC-*s*-MSN and ~20% with PEG_1-FITC-*s*-MSN) showed a significantly better

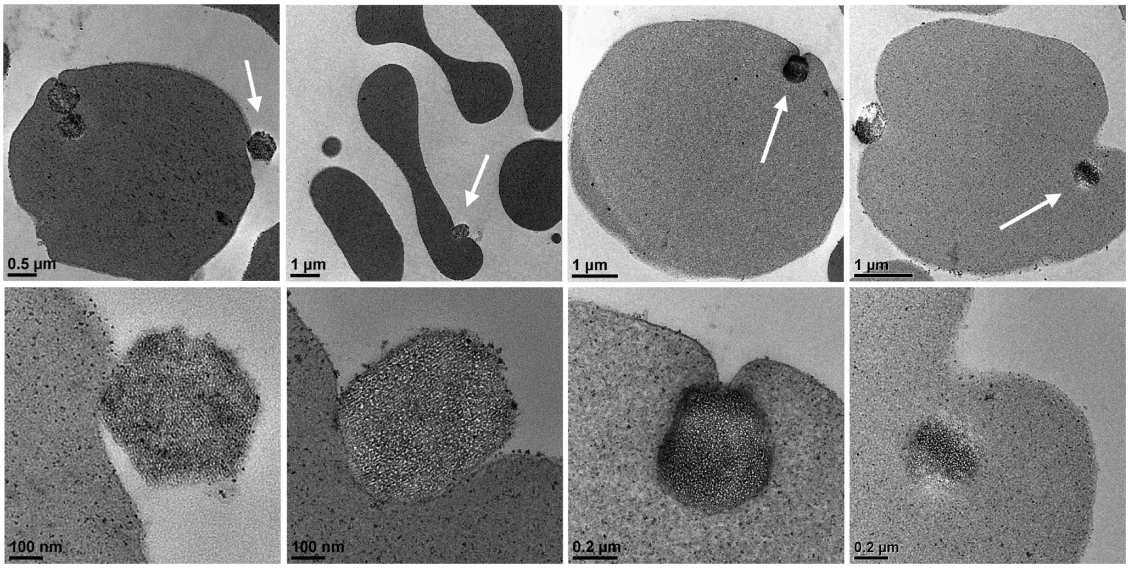

Figure 5. Cellular uptake process (left to right) examined by transmission electron microscopy of RBCs (5% hematocrit) incubated with 20 μg mL^{-1} *l*-MSN. Images increase in magnification from top to bottom, with features highlighted in white arrows. These images (left to right) correspond to different cells at different stages of nanoparticle encapsulation.

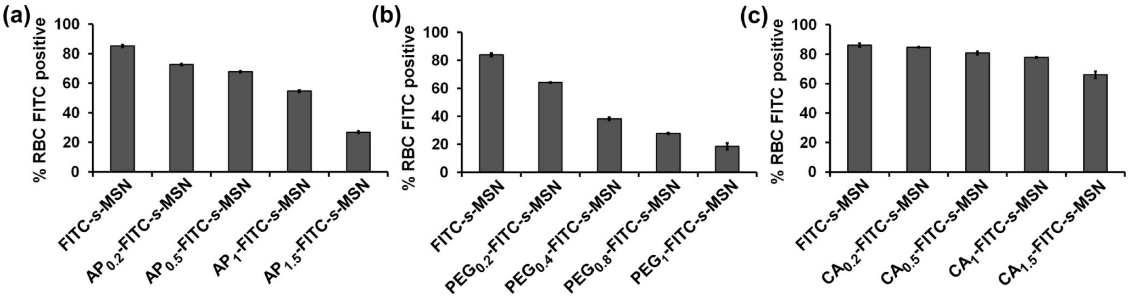

Figure 6. Flow cytometry measurement of RBCs (5×10^6 cells mL^{-1}) incubated with 10 μg mL^{-1} of (a) AP$_x$-FITC-*s*-MSN, (b) PEG$_x$-FITC-*s*-MSN, and (c) CA$_x$-FITC-*s*-MSN.

ability to reduce the MSN binding with RBC than CA groups (~65% of RBC bound with $CA_{1.5}$-FITC-*s*-MSN). The inhibitory effect of PEG on the adsorption of MSN to RBC was not surprising since PEGylation of nanoparticles is generally used to block nonspecific binding of nanoparticles to proteins.[54] On the contrary, the reduction of MSN binding to RBC due to aminopropyl group functionalization was completely unexpected because amines are well-known to facilitate adsorption of several biomolecules to the surface of nanoparticles and facilitate many nanoparticle−cell interactions.[34,55] The reduced binding of AP-FITC-*s*-MSN to RBC could be explained by the electrostatic interaction between amino groups on the surface of MSNs and surface silanols,[56] which diminishes the accessibility of silanol groups to the cell membrane.

The results obtained by flow cytometry were further confirmed by examination of the mixtures of the derivatized MSNs with RBCs under confocal fluorescence microscopy. For this purpose, RBCs were first labeled with PKH26 red fluorescent dye (Sigma) and incubated with FITC-labeled particles at the same conditions as in the flow cytometry experiment. FITC-*l*-MSNs, FITC-*s*-MSNs, and $CA_{1.5}$-FITC-*s*-MSNs (Figure 7a,b,e) were easily observed associated to PKH26-labeled RBCs. Conversely, only a small proportion of $AP_{1.5}$-FITC-*s*-MSNs (Figure 7c) and PEG_1-FITC-*s*-MSNs (Figure 7d) were found colocalized with PKH26-RBCs, while most of the particles were observed in the extracellular space. A series of movies showing each one of these combinations of MSNs and RBCs were prepared from micrographs taken at different *z*-positions by changing the focal plane every 0.5 μm; these movies can be found in the Supporting Information. The different affinities of each MSN for the RBCs were also confirmed by the different shifts of the green fluorescence intensities in the 2D dot plots from flow cytometry (Figure 7, bottom).

Effect of RBC−MSN Interaction on RBC Deformability. The attachment of nanoparticles to the surface of red blood cells has been suggested for extending the circulation time and sustained release of therapeutic agents.[40,53] Such attachment, however, could have an impact on the properties of the membrane affecting the normal function of RBCs. Surprisingly, this potential problem has not been addressed for any nanoparticle-based drug carrier, to the best of our knowledge. One of the key properties of RBCs (6−8 μm in diameter) is their

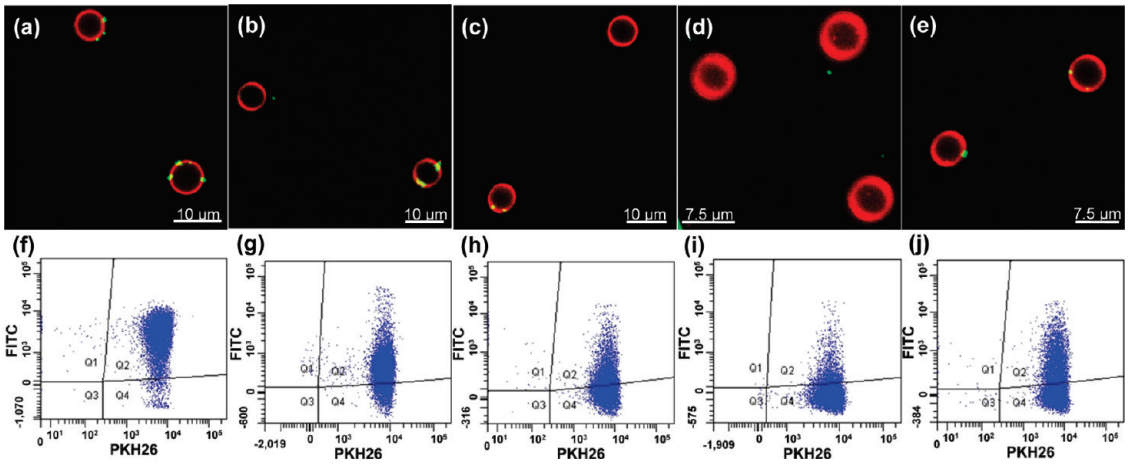

Figure 7. Confocal fluorescence micrographs (top) and dot plots from the flow cytometry analyses (bottom) of PKH26-labeled RBCs (5×10^6 cells mL^{-1}) incubated with 10 μg mL^{-1} of (a,f) FITC-*l*-MSN, (b,g) FITC-*s*-MSN, (c,h) $AP_{1.5}$-FITC-*s*-MSN, (d,i) PEG_1-FITC-*s*-MSN, and (e,j) $CA_{1.5}$-FITC-*s*-MSN. The axes correspond to the intensity of red fluorescence due to PKH26 labeling (horizontal axis) and green fluorescence due to the attachment of FITC-MSNs onto PKH26-RBCs (vertical axis). The plot was gated to show PKH26-labeled RBCs in area Q4 and FITC fluorescent PKH26-RBCs in area Q2. Individual channels for the merged confocal images and enlarged dot plots with PKH26-RBC control are shown in Supporting Information Figure S7 and Figure S8, respectively.

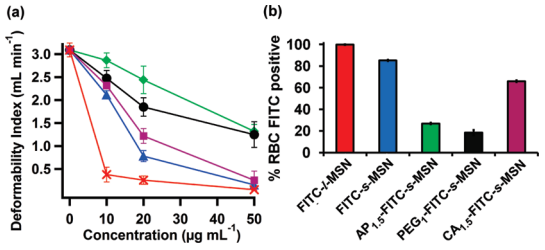

Figure 8. (a) Deformability index (DI) of RBCs incubated with *s*-MSN (blue), $AP_{1.5}$-*s*-MSN (green), PEG_1-*s*-MSN (black), $CA_{1.5}$-*s*-MSN (purple), and *l*-MSN (red). (b) Flow cytometry analyses of RBCs incubated with FITC-*l*-MSN (red), FITC-*s*-MSN (blue), $AP_{1.5}$-FITC-*s*-MSN (green), PEG_1-FITC-*s*-MSN (black), and $CA_{1.5}$-FITC-*s*-MSN (purple).

ability to undergo deformation to traverse the capillaries of the microvascular system (2−3 μm in diameter). This remarkable deformability of RBCs is critical for effective blood flow and depends strongly on the flexibility of the cell membrane. This is the reason why it is important to assess the effects of MSN attachment on the deformability of RBCs.

To study the deformability of RBCs, we used a literature reported method consisting of filtering the cells through polycarbonate membranes with straight channels of 3 μm pore diameter (Nucleopore).[41] This technique is generally accepted as a relative indication of RBC deformability.[41,57−59] We measured the filterability of fresh human RBCs (5% hematocrit) previously incubated with varying concentrations (10, 20, 50 μg mL^{-1}) of MSN under a constant negative pressure (−20 cm H_2O). The time it took each RBC suspension to flow through the membrane was recorded and the deformability index (DI) was expressed as the volume (mL) of red blood cells filtered per minute. As shown in Figure 8a, the deformability of RBC decreased with increasing concentrations of all MSN materials. The RBC deformability was severely impaired by *l*-MSN at concentrations as low as 10 μg mL^{-1}. This result is not surprising given the strong affinity and shape altering effects already described for *l*-MSN. As expected, the incorporation of AP and PEG groups to the surface of *s*-MSN preserved the elasticity of RBCs better than the nonfunctionalized *s*-MSN and the CA-*s*-MSN, especially at the higher concentrations (>20 μg mL^{-1}). These results correlate well with the observed effects on the degree of RBC−MSN interactions (Figure 8b). These observations suggest that the attachment of MSNs to the surface of RBCs restricts the flexibility of the membrane and leads to impairment in the deformability of RBCs. Conversely, the attachment of functional groups to the surface of MSNs reduces the affinity of the particles to the membrane of RBC and allows the cells to preserve their deformability.

CONCLUSION

In this study, we investigated the interactions between MSNs of different particle sizes and surface properties and RBC membranes by using fluorescence and electron microscopies and cell biology techniques. We compared the size- and surface-dependent hemocompatibility of two types of MSN materials (MCM-41 and SBA-15) and showed, for the first time, how MSNs are engulfed by RBCs. This size- and surface-dependent process is the resultant of two opposing forces, namely, the attractive interaction between MSNs and RBCs and the bending of the cell membrane. These results suggest that only small MCM-41-type MSN materials (100−200 nm) may be considered as potentially safe candidates for intravascular drug delivery. It must be noted that, although RBCs are the dominant cells in blood, the interactions of these nanoparticles with other blood cells and components[60,61] should also be

evaluated to ensure the safe use of these materials for biomedical applications. In addition, we demonstrated that the biocompatibility of these MSN materials with RBCs strongly depends on their surface derivatization to minimize their interaction with red blood cells. Blocking the surface silanols of the particles with organic groups reduces their interactions with the membranes of RBCs. Minimizing these interactions has a dramatic effect on preserving the deformability of RBCs, which is necessary to ensure effective blood circulation. These findings suggest that it is possible to gain control over the interactions of MSNs with RBC membranes in order to regulate their circulation half-lives for various therapeutic purposes, while minimizing their toxicity by carefully choosing and tuning their surface functionalities. As new MSN-based drug delivery systems burgeon from many international research groups, our results will provide a practical guide to size and surface considerations when designing MSN-based drug carriers for delivery, diagnostic, and therapeutic applications.

METHODS

Synthesis of Mesoporous Silica Nanoparticles. *s*-MSN was prepared by our previously reported method.[33] In brief, *N*-cetyltrimethylammonium bromide (CTAB, 1.00 g, 2.74 mmol) was dissolved in 480 mL of nanopure water, followed by the addition of 3.5 mL of sodium hydroxide aqueous solution (2.0 M), and the mixture was heated to 80 °C. Tetraethoxysilane (TEOS, 5.0 mL, 22.4 mmol) was added dropwise to the surfactant solution under vigorous stirring. The reaction mixture was stirred at 80 °C for another 2 h. The resulting white solid was filtered, washed thoroughly with water and methanol, and dried under high vacuum at 80 °C overnight. The fluorescent-labeled MSN (FITC-*s*-MSN) was synthesized by reacting fluorescein isothiocyanate (FITC, 15 mg, 38.5 μmol) with (3-aminopropyl)trimethoxysilane (APTMS, 10 μL, 57.3 μmol) for 2 h in dimethyl sulfoxide (DMSO) and adding the resulting product following the addition of TEOS in the above synthesis. The unlabeled FITC was removed by Soxhlet extraction with methanol. The amount of FITC labeled on FITC-*s*-MSN was quantified to be 20−30 μmol g^{-1} by TGA. The functionalization of *s*-MSN and FITC-*s*-MSN with aminopropyl (AP), polyethylene glycol (PEG), and carboxylate (CA) groups was performed by refluxing a suspension of the as-made material (200 mg of *s*-MSN or FITC-*s*-MSN) with APTMS, 2-[methoxy(polyethylenoxy)propyl]trimethoxysilane (PEG-silane), and 3-(triethoxysilyl)propylsuccinic anhydride of various amount (*x* mmol) in anhydrous toluene (50 mL) for 20 h, followed by filtration and washing with toluene and methanol, and dried under high vacuum overnight. The succinic anhydride groups were hydrolyzed by boiling the materials in water for 6 h and measured by FTIR. The CTAB surfactant was removed by refluxing the materials in 0.37% HCl methanol, followed by filtration and washing with abundant methanol and dried under high vacuum. The amount of functional groups (AP, PEG, and CA) grafted on MSNs was quantified by TGA shown in the bottom of Figure S5 and summarized in Table S1.

l-MSN was prepared by a modified literature procedure.[5] Pluronic P104 (courtesy of BASF, 7.0 g) was dissolved in a mixture of water (164 g) and HCl (109 g, 4M) and stirred at 55 °C for 1 h. Tetramethyl orthosilicate (10.64 g) was quickly added into the solution at 55 °C. After continuous stirring for 24 h, the reaction mixture was moved to a Teflon-lined, high-pressure autoclave for further hydrothermal treatment at 150 °C for 24 h. The product was isolated by filtration, washed with copious water and methanol, and dried at 80 °C in air. The Pluronic P104 surfactant was removed by calcination at 550 °C for 6 h. The *l*-MSN was fluorescently labeled (FITC-*l*-MSN) by reacting FITC (15 mg, 38.5 μmol) with APTMS (10 μL, 57.3 μmol) for 2 h in dimethyl sulfoxide (DMSO) and adding the resulting product to a suspension of *l*-MSN (1 g) in anhydrous toluene (100 mL) for 20 h, followed by filtration and washing with toluene and methanol. The unlabeled FITC was removed by Soxhlet extraction with methanol as the solvent. The amount of FITC labeled on FITC-*l*-MSN was quantified to be around 30 μmol g^{-1}.

The products were characterized by X-ray diffraction in a Rigaku Ultima IV diffractometer, nitrogen sorption analysis in a Micromeritics Tristar 3000 surface area, and porosity analyzer using Brunauer−Emmett−Teller (BET) equation to calculate apparent surface area and pore volume and the Barret−Joyner−Halenda (BJH) method to calculate pore size distribution, thermogravimetric analysis (TGA) in a TGA 2950 thermogravimetric analyzer with a temperature ramp of 5 °C/min in air, dynamic light scattering size analyses of particle suspensions in a Malvern Nano HT Zetasizer, scanning electron microscopy (SEM) of samples coated with gold in a FEI Quanta 250 FEG microscope, and transmission electron microscopy (TEM) of samples supported on copper grids in a Tecnai G2 F20 microscope operated at 200 kV. FTIR spectroscopy was performed using a Nicolet Nexus 470 (Madison, EI), equipped with a cooled CT/A detector and an Ever-Glo source.

Isolation and Labeling of Red Blood Cells (RBCs). Ethylenediamine tetraacetic acid (EDTA)-stabilized human blood samples were freshly collected in the Occupational Medicine Office of Iowa State University and Ames Laboratory. Whole blood was centrifuged at 1600 rpm for 5 min, and the plasma, buffy coat, and top layer of cells were decanted. The remaining packed RBCs were washed five times with sterile isotonic PBS. For labeling with PKH26 (red fluorescent cell linker kit, Sigma, USA), 100 μL of packed RBCs was resuspended in 1 mL of diluent C and mixed with 1 mL of diluent C containing 4 μM PKH26. Cells were incubated for 5 min at room temperature in the dark. The reaction was stopped by adding 1 mL of plasma (heat inactivated for 1 h at 65 °C beforehand) for 1 min and centrifuged at 1600 rpm for 5 min. The stained RBCs were washed five times with PBS to remove free pKH26 dye.

Hemolysis Assay. After cell washing, 200 μL of packed RBC was diluted to 4 mL with PBS (5% hematocrit). The diluted RBC suspension (0.2 mL) was then mixed with *s*-MSN and *l*-MSN suspensions in PBS (0.8 mL) at various concentrations. PBS and water (0.8 mL) were used instead of MSN suspensions as negative and positive control, respectively. The mixture was gently vortexed and incubated at room temperature for 2 h, followed by centrifuge (1600 rpm, 5 min), and the absorbance of the supernatant at 541 nm was measured by UV−visible spectrometry. The percent hemolysis of RBCs was calculated using the following formula: percent hemolysis = ((sample absorbance − negative control absorbance)/(positive control absorbance − negative control absorbance)) × 100.

Scanning Electron Microscopy (SEM). The diluted RBC suspension (5% hematocrit, 0.2 mL) was mixed with *s*-MSN and *l*-MSN suspensions in PBS (0.8 mL) at various concentrations and incubated at room temperature for 2 h. The samples were then fixed by adding a 1% glutaraldehyde solution dropwise over 5 min and further incubated at 37 °C for 1.5 h, followed by postfixation with 1% osmium tetroxide in PBS for 1.5 h. Cells were dehydrated in increasing concentrations of ethanol (50, 60 70, 80, 90, and 100%) for 15 min each. The cell suspensions were dropped onto glass coverslips, dried, and coated with Au before viewing under a FEI Quanta 250 FEG scanning electron microscope.

Transmission Electron Microscopy (TEM). The samples were prepared, fixed, and dehydrated as above and stained with 2% uranyl acetate in 70% ethanol at room temperature overnight. The cells were washed three times with acetone and embedded in Epon. The embedded samples were sectioned in 60 nm thick slices on a sliding ultramicrotome. Thin sections supported on copper grids were examined in a Tecnai G2 F20 microscope operated at 200 kV.

Flow Cytometry. After cell washing, 200 μL of RBC suspension at 5×10^6 cells mL^{-1} was mixed with 200 μL of FITC-MSN suspensions in PBS at 20 μg mL^{-1} and incubated at room temperature for 2 h before flow cytometry analysis in a BD FACSCanto instrument.

Confocal Fluorescence Microscopy. PKH26-labeled RBC suspension (200 μL) at 5×10^6 cells mL^{-1} was mixed with 200 μL of FITC-MSN suspensions in PBS at 20 μg mL^{-1} and incubated at room temperature for 2 h. An aliquot of sample was mounted between plastic coverslips and imaged in a Leica SP5 X confocal system.

Deformability Assay. Packed RBCs (1.5 mL) were washed and diluted to 30 mL with PBS (5% hematocrit). The diluted RBC suspension (1 mL) was then mixed with MSN suspensions in PBS (4 mL) at various final concentrations of 10, 20, and 50 μg mL^{-1} with PBS as control. The mixture was gently vortexed and incubated at room temperature for 2 h before filtering through polycarbonate membrane with straight channels of 3 μm pore diameter (Nucleopore, Fisher, USA) under a constant negative pressure (−20 cm H_2O). The time for 0.5 mL RBC suspension to pass through the membrane was recorded, and the deformability index (DI) was calculated as the volume of red blood cells filtered per minute. Data were presented as mean values of triplicate experiments. The present method and apparatus for RBC filterability measurement have been described in detail elsewhere.[41]

Acknowledgment. This manuscript has been dedicated in memory of our dear mentor and friend, Victor S.-Y. Lin. This research is supported by the U.S. National Science Foundation NSF (CHE-0809521).

Supporting Information Available: The characterizations of MSNs, additional SEM images of RBCs with MSNs, dose-dependent RBC hemolysis and spiculation by *l*-MSN, enlarged confocal fluorescence micrographs, dot plots from flow cytometry, and movies of confocal micrographs recorded at different *z*-positions. This material is available free of charge *via* the Internet at http://pubs.acs.org.

REFERENCES AND NOTES

1. Slowing, I. I.; Vivero-Escoto, J. L.; Trewyn, B. G.; Lin, V. S. Y. Mesoporous Silica Nanoparticles: Structural Design and Applications. *J. Mater. Chem.* **2010,** *20*, 7924–7937.
2. Cai, Q.; Lin, W. Y.; Xiao, F. S.; Pang, W. Q.; Chen, X. H.; Zou, B. S. The Preparation of Highly Ordered MCM-41 with Extremely Low Surfactant Concentration. *Microporous Mesoporous Mater.* **1999,** *32*, 1–15.
3. Huh, S.; Wiench, J. W.; Yoo, J.-C.; Pruski, M.; Lin, V. S. Y. Organic Functionalization and Morphology Control of Mesoporous Silicas *via* a Co-condensation Synthesis Method. *Chem. Mater.* **2003,** *15*, 4247–4256.
4. Lu, F.; Wu, S.-H.; Hung, Y.; Mou, C.-Y. Size Effect on Cell Uptake in Well-Suspended, Uniform Mesoporous Silica Nanoparticles. *Small* **2009,** *5*, 1408–1413.
5. Linton, P.; Alfredsson, V. Growth and Morphology of Mesoporous SBA-15 Particles. *Chem. Mater.* **2008,** *20*, 2878–2880.
6. Descalzo, A. B.; Martinez-Manez, R.; Sancenon, F.; Hoffmann, K.; Rurack, K. The Supramolecular Chemistry of Organic−Inorganic Hybrid Materials. *Angew. Chem., Int. Ed.* **2006,** *45*, 5924–5948.
7. Coti, K. K.; Belowich, M. E.; Liong, M.; Ambrogio, M. W.; Lau, Y. A.; Khatib, H. A.; Zink, J. I.; Khashab, N. M.; Stoddart, J. F. Mechanised Nanoparticles for Drug Delivery. *Nanoscale* **2009,** *1*, 16–39.
8. Zhao, Y.; Vivero-Escoto, J. L.; Slowing, I. I.; Trewyn, B. G.; Lin, V. S. Y. Capped Mesoporous Silica Nanoparticles as Stimuli-Responsive Controlled Release Systems for Intracellular Drug/Gene Delivery. *Expert Opin. Drug Delivery* **2010,** *7*, 1013–1029.
9. Shen, S.; Chow, P. S.; Chen, F.; Tan, R. B. H. Submicron Particles of SBA-15 Modified with MgO as Carriers for Controlled Drug Delivery. *Chem. Pharm. Bull.* **2007,** *55*, 985–991.
10. Vivero-Escoto, J. L.; Slowing, I. I.; Trewyn, B. G.; Lin, V. S. Y. Mesoporous Silica Nanoparticles for Intracellular Controlled Drug Delivery. *Small* **2010,** *6*, 1952–1967.
11. Slowing, I. I.; Trewyn, B. G.; Lin, V. S. Y. Mesoporous Silica Nanoparticles for Intracellular Delivery of Membrane-Impermeable Proteins. *J. Am. Chem. Soc.* **2007,** *129*, 8845–8849.
12. Kim, S.-I.; Pham, T. T.; Lee, J.-W.; Roh, S.-H. Releasing Properties of Proteins on SBA-15 Spherical Nanoparticles Functionalized with Aminosilanes. *J. Nanosci. Nanotechnol.* **2010,** *10*, 3467–3472.
13. Nguyen, T. P. B.; Lee, J.-W.; Shim, W. G.; Moon, H. Synthesis of Functionalized SBA-15 with Ordered Large Pore Size and Its Adsorption Properties of Bovine Serum Albumin. *Microporous Mesoporous Mater.* **2008,** *110*, 560–569.
14. Doadrio, J. C.; Sousa, E. M. B.; Izquierdo-Barba, I.; Doadrio, A. L.; Perez-Pariente, J.; Vallet-Regi, M. Functionalization of Mesoporous Materials with Long Alkyl Chains as a Strategy for Controlling Drug Delivery Pattern. *J. Mater. Chem.* **2006,** *16*, 462–466.
15. Zhu, Y.; Kaskel, S.; Ikoma, T.; Hanagata, N. Magnetic SBA-15/Poly(*N*-isopropylacrylamide) Composite: Preparation, Characterization and Temperature-Responsive Drug Release Property. *Microporous Mesoporous Mater.* **2009,** *123*, 107–112.
16. Mercuri, L. P.; Carvalho, L. V.; Lima, F. A.; Quayle, C.; Fantini, M. C. A.; Tanaka, G. S.; Cabrera, W. H.; Furtado, M. F. D.; Tambourgi, D. V.; Matos, J. d. R.; *et al.*Ordered Mesoporous Silica SBA-15: A New Effective Adjuvant To Induce Antibody Response. *Small* **2006,** *2*, 254–256.
17. Zhao, Y.; Trewyn, B. G.; Slowing, I. I.; Lin, V. S. Y. Mesoporous Silica Nanoparticle-Based Double Drug Delivery System for Glucose-Responsive Controlled Release of Insulin and Cyclic AMP. *J. Am. Chem. Soc.* **2009,** *131*, 8398–8400.
18. Lee, J. E.; Lee, N.; Kim, H.; Kim, J.; Choi, S. H.; Kim, J. H.; Kim, T.; Song, I. C.; Park, S. P.; Moon, W. K.; *et al.*Uniform Mesoporous Dye-Doped Silica Nanoparticles Decorated with Multiple Magnetite Nanocrystals for Simultaneous Enhanced Magnetic Resonance Imaging, Fluorescence Imaging, and Drug Delivery. *J. Am. Chem. Soc.* **2010,** *132*, 552–557.
19. Liong, M.; Lu, J.; Kovochich, M.; Xia, T.; Ruehm, S. G.; Nel, A. E.; Tamanoi, F.; Zink, J. I. Multifunctional Inorganic Nanoparticles for Imaging, Targeting, and Drug Delivery. *ACS Nano* **2008,** *2*, 889–896.
20. Tu, H.-L.; Lin, Y.-S.; Lin, H.-Y.; Hung, Y.; Lo, L.-W.; Chen, Y.-F.; Mou, C.-Y. *In Vitro* Studies of Functionalized Mesoporous Silica Nanoparticles for Photodynamic Therapy. *Adv. Mater.* **2009,** *21*, 172–177.
21. Taylor, K. M. L.; Kim, J. S.; Rieter, W. J.; An, H.; Lin, W.; Lin, W. Mesoporous Silica Nanospheres as Highly Efficient MRI Contrast Agents. *J. Am. Chem. Soc.* **2008,** *130*, 2154–2155.
22. Lee, C.-H.; Cheng, S.-H.; Wang, Y.-J.; Chen, Y.-C.; Chen, N.-T.; Souris, J.; Chen, C.-T.; Mou, C.-Y.; Yang, C.-S.; Lo, L.-W. Near-Infrared Mesoporous Silica Nanoparticles for Optical Imaging: Characterization and *In Vivo* Biodistribution. *Adv. Funct. Mater.* **2009,** *19*, 215–222.
23. Lu, J.; Liong, M.; Li, Z.; Zink, J. I.; Tamanoi, F. Biocompatibility, Biodistribution, and Drug-Delivery Efficiency of Mesoporous Silica Nanoparticles for Cancer Therapy in Animals. *Small* **2010,** *6*, 1794–1805.
24. Kim, J.; Kim, H. S.; Lee, N.; Kim, T.; Kim, H.; Yu, T.; Song, I. C.; Moon, W. K.; Hyeon, T. Multifunctional Uniform Nanoparticles Composed of a Magnetite Nanocrystal Core and a Mesoporous Silica Shell for Magnetic Resonance and Fluorescence Imaging and for Drug Delivery. *Angew. Chem., Int. Ed.* **2008,** *47*, 8438–8441.
25. Meng, H.; Liong, M.; Xia, T.; Li, Z.; Ji, Z.; Zink, J. I.; Nel, A. E. Engineered Design of Mesoporous Silica Nanoparticles to Deliver Doxorubicin and P-Glycoprotein siRNA To Overcome Drug Resistance in a Cancer Cell Line. *ACS Nano* **2010,** *4*, 4539–4550.
26. Tao, Z.; Morrow, M. P.; Asefa, T.; Sharma, K. K.; Duncan, C.; Anan, A.; Penefsky, H. S.; Goodisman, J.; Souid, A.-K. Mesoporous Silica Nanoparticles Inhibit Cellular Respiration. *Nano Lett.* **2008,** *8*, 1517–1526.
27. Hudson, S. P.; Padera, R. F.; Langer, R.; Kohane, D. S. The Biocompatibility of Mesoporous Silicates. *Biomaterials* **2008,** *29*, 4045–4055.

28. Heikkilae, T.; Santos, H. A.; Kumar, N.; Murzin, D. Y.; Salonen, J.; Laaksonen, T.; Peltonen, L.; Hirvonen, J.; Lehto, V.-P. Cytotoxicity Study of Ordered Mesoporous Silica MCM-41 and SBA-15 Microparticles on Caco-2 Cells. *Eur. J. Pharm. Biopharm.* **2010,** *74*, 483–494.
29. Al Shamsi, M.; Al Samri, M. T.; Al-Salam, S.; Conca, W.; Shaban, S.; Benedict, S.; Tariq, S.; Biradar, A. V.; Penefsky, H. S.; Asefa, T.; *et al.*Biocompatibility of Calcined Mesoporous Silica Particles with Cellular Bioenergetics in Murine Tissues. *Chem. Res. Toxicol.* **2010,** *23*, 1796–1805.
30. Slowing, I. I.; Wu, C.-W.; Vivero-Escoto, J. L.; Lin, V. S. Y. Mesoporous Silica Nanoparticles for Reducing Hemolytic Activity towards Mammalian Red Blood Cells. *Small* **2009,** *5*, 57–62.
31. Lin, Y.-S.; Haynes, C. L. Impacts of Mesoporous Silica Nanoparticle Size, Pore Ordering, and Pore Integrity on Hemolytic Activity. *J. Am. Chem. Soc.* **2010,** *132*, 4834–4842.
32. Lin, Y.-S.; Haynes, C. L. Synthesis and Characterization of Biocompatible and Size-Tunable Multifunctional Porous Silica Nanoparticles. *Chem. Mater.* **2009,** *21*, 3979–3986.
33. Lai, C.-Y.; Trewyn, B. G.; Jeftinija, D. M.; Jeftinija, K.; Xu, S.; Jeftinija, S.; Lin, V. S. Y. A Mesoporous Silica Nanosphere-Based Carrier System with Chemically Removable CdS Nanoparticle Caps for Stimuli-Responsive Controlled Release of Neurotransmitters and Drug Molecules. *J. Am. Chem. Soc.* **2003,** *125*, 4451–4459.
34. Slowing, I.; Trewyn, B. G.; Lin, V. S. Y. Effect of Surface Functionalization of MCM-41-Type Mesoporous Silica Nanoparticles on the Endocytosis by Human Cancer Cells. *J. Am. Chem. Soc.* **2006,** *128*, 14792–14793.
35. Radu, D. R.; Lai, C.-Y.; Huang, J.; Shu, X.; Lin, V. S. Y. Fine-Tuning the Degree of Organic Functionalization of Mesoporous Silica Nanosphere Materials *via* an Interfacially Designed Co-condensation Method. *Chem. Commun.* **2005,** 1264–1266.
36. Radu, D. R.; Lai, C.-Y.; Jeftinija, K.; Rowe, E. W.; Jeftinija, S.; Lin, V. S. Y. A Polyamidoamine Dendrimer-Capped Mesoporous Silica Nanosphere-Based Gene Transfection Reagent. *J. Am. Chem. Soc.* **2004,** *126*, 13216–13217.
37. Hom, C.; Lu, J.; Liong, M.; Luo, H.; Li, Z.; Zink, J. I.; Tamanoi, F. Mesoporous Silica Nanoparticles Facilitate Delivery of siRNA To Shutdown Signaling Pathways in Mammalian Cells. *Small* **2010,** *6*, 1185–1190.
38. Torney, F.; Trewyn, B. G.; Lin, V. S. Y.; Wang, K. Mesoporous Silica Nanoparticles Deliver DNA and Chemicals into Plants. *Nat. Nanotechnol.* **2007,** *2*, 295–300.
39. Wang, L.-S.; Wu, L.-C.; Lu, S.-Y.; Chang, L.-L.; Teng, I. T.; Yang, C.-M.; Ho, J.-a. A. Biofunctionalized Phospholipid-Capped Mesoporous Silica Nanoshuttles for Targeted Drug Delivery: Improved Water Suspensibility and Decreased Nonspecific Protein Binding. *ACS Nano* **2010,** *4*, 4371–4379.
40. Chambers, E.; Mitragotri, S. Prolonged Circulation of Large Polymeric Nanoparticles by Non-covalent Adsorption on Erythrocytes. *J. Controlled Release* **2004,** *100*, 111–119.
41. Reid, H. L.; Barnes, A. J.; Lock, P. J.; Dormandy, J. A.; Dormandy, T. L. A Simple Method for Measuring Erythrocyte Deformability. *J. Clin. Pathol.* **1976,** *29*, 855–8.
42. Yawata, Y. *Cell Membrane: the Red Blood Cell as a Model*; Wiley-VCH: Weinheim, Germany, 2003; pp 38−40.
43. Roiter, Y.; Ornatska, M.; Rammohan, A. R.; Balakrishnan, J.; Heine, D. R.; Minko, S. Interaction of Nanoparticles with Lipid Membrane. *Nano Lett.* **2008,** *8*, 941–944.
44. Lipowsky, R.; Dobereiner, H. G. Vesicles in Contact with Nanoparticles and Colloids. *Europhys. Lett.* **1998,** *43*, 219–225.
45. Deserno, M.; Gelbart, W. M. Adhesion and Wrapping in Colloid-Vesicle Complexes. *J. Phys. Chem. B* **2002,** *106*, 5543–5552.
46. Fleck, C. C.; Netz, R. R. Electrostatic Colloid−Membrane Binding. *Europhys. Lett.* **2004,** *67*, 314–320.
47. Reynwar, B. J.; Illya, G.; Harmandaris, V. A.; Mueller, M. M.; Kremer, K.; Deserno, M. Aggregation and Vesiculation of Membrane Proteins by Curvature-Mediated Interactions. *Nature* **2007,** *447*, 461–464.
48. Zhu, H. Y.; Zhao, X. S.; Lu, G. Q.; Do, D. D. Improved Comparison Plot Method for Pore Structure Characterization of MCM-41. *Langmuir* **1996,** *12*, 6513–6517.
49. Giri, S.; Trewyn, B. G.; Stellmaker, M. P.; Lin, V. S. Y. Stimuli-Responsive Controlled-Release Delivery System Based on Mesoporous Silica Nanorods Capped with Magnetic Nanoparticles. *Angew. Chem., Int. Ed.* **2005,** *44*, 5038–5044.
50. Vivero-Escoto, J. L.; Slowing, I. I.; Wu, C.-W.; Lin, V. S. Y. Photoinduced Intracellular Controlled Release Drug Delivery in Human Cells by Gold-Capped Mesoporous Silica Nanosphere. *J. Am. Chem. Soc.* **2009,** *131*, 3462–3463.
51. Zhu, C.-L.; Song, X.-Y.; Zhou, W.-H.; Yang, H.-H.; Wen, Y.-H.; Wang, X.-R. An Efficient Cell-Targeting and Intracellular Controlled-Release Drug Delivery System Based on MSN-PEM-Aptamer Conjugates. *J. Mater. Chem.* **2009,** *19*, 7765–7770.
52. He, Q.; Zhang, Z.; Gao, Y.; Shi, J.; Li, Y. Intracellular Localization and Cytotoxicity of Spherical Mesoporous Silica Nano- and Microparticles. *Small* **2009,** *5*, 2722–2729.
53. Hall, S. S.; Mitragotri, S.; Daugherty, P. S. Identification of Peptide Ligands Facilitating Nanoparticle Attachment to Erythrocytes. *Biotechnol. Prog.* **2007,** *23*, 749–754.
54. He, Q.; Zhang, J.; Shi, J.; Zhu, Z.; Zhang, L.; Bu, W.; Guo, L.; Chen, Y. The Effect of PEGylation of Mesoporous Silica Nanoparticles on Nonspecific Binding of Serum Proteins and Cellular Responses. *Biomaterials* **2010,** *31*, 1085–1092.
55. Gao, F.; Botella, P.; Corma, A.; Blesa, J.; Dong, L. Monodispersed Mesoporous Silica Nanoparticles with Very Large Pores for Enhanced Adsorption and Release of DNA. *J. Phys. Chem. B* **2009,** *113*, 1796–1804.
56. Caravajal, G. S.; Leyden, D. E.; Quinting, G. R.; Maciel, G. E. Structural Characterization of (3-Aminopropyl)triethoxysilane-Modified Silicas by Silicon-29 and Carbon-13 Nuclear Magnetic Resonance. *Anal. Chem.* **1988,** *60*, 1776–86.
57. Luquita, A.; Urli, L.; Svetaz, M. J.; Gennaro, A. M.; Giorgetti, M. E.; Pistone, G.; Volpintesta, R.; Palatnik, S.; Rasia, M. *In Vitro* and *Ex Vivo* Effect of Hyaluronic Acid on Erythrocyte Flow Properties. *J. Biomed. Sci.* **2010,** *17*, 1–7.
58. Brown Clinton, D.; Ghali Halim, S.; Zhao, Z.; Thomas, L. L.; Friedman, E. A. Association of Reduced Red Blood Cell Deformability and Diabetic Nephropathy. *Kidney Int.* **2005,** *67*, 295–300.
59. Kikuchi, Y.; Koyama, T. Red Blood Cell Deformability and Protein Adsorption on Red Blood Cell Surface. *Am. J. Physiol.* **1984,** *247*, H739–H747.
60. De Paoli Lacerda, S. H.; Park, J.-J.; Meuse, C.; Pristinski, D.; Becker, M. L.; Karim, A.; Douglas, J. F. Interaction of Gold Nanoparticles with Common Human Blood Proteins. *ACS Nano* **2010,** *4*, 365–379.
61. Semberova, J.; De Paoli Lacerda, S. H.; Simakova, O.; Holada, K.; Gelderman, M. P.; Simak, J. Carbon Nanotubes Activate Blood Platelets by Inducing Extracellular Ca^{2+} Influx Sensitive to Calcium Entry Inhibitors. *Nano Lett.* **2009,** *9*, 3312–3317.